Off-Grid Space-Frequency Environment Sensing for Next Generation Cognitive Radars

Augusto Aubry
DIETI
University of Naples "Federico II"
Napoli, Italy
augusto.aubry@unina.it

Prabhu Babu
CARE
Indian Institute of Tech. Delhi
New Delhi, India
prabhubabu@care.iitd.ac.in

Antonio De Maio
DIETI
University of Naples "Federico II"
Napoli, Italy
ademaio@unina.it

Luca Pallotta
DiING
University of Basilicata
Potenza, Italy
luca.pallotta@unibas.it

***Abstract*—This paper proposes a novel 2-D spectrum sensing method to improve environmental awareness capabilities compared with traditional grid-based techniques. Instead of using fixed angles of arrival (AOA), as dictated by a grid of points, the off-grid approaches allow for flexibility in estimating angle displacements at a reduced computational complexity increase. The recovery process is formulated as a regularized maximum likelihood (RML) estimation, leveraging block-sparsity. The optimization is tackled with a maximum block improvement (MBI) method to estimate noise power, the 2-D profile, and angular displacements. Moreover, two refinement strategies are used to improve the angle estimation accuracy. The method is validated through numerical simulations modeling realistic environments.**

***Index Terms*—off-grid angle of arrival (AOA), cognitive radar, maximum block improvement (MBI), spectrum sensing.**

I. Introduction

Spectral cognition is essential for next-generation cognitive radars, which use the perception-action cycle [1], [2] to ensure spectral coexistence with other radio frequency (RF) systems while providing adequate surveillance capabilities [3], [4]. This requires environmental awareness of the operational scenario, obtained through dynamic inference of the spectrum occupancy, as demanded by a flexible and wise exploitation of the frequency resources. In particular, precise information about the location of emitters in both the frequency and angular domains enables more efficient use of space-time system resources and, not surprisingly, a multitude of spectrum sensing strategies have been devised possibly facing with multiple domains of interest [5]–[8].

Recently, advanced techniques leveraging sparsity-based signal processing tools to infer space-frequency state with a better reliability than traditional methods have been proposed, exploiting the usually met assumption of a limited number of operating emitters in the monitored scene [9]. In this respect, in [10] a two-dimensional (2-D) spectrum sensing algorithms that capitalize on block sparsity during the recovery process, extending the sparse learning via iterative minimization (SLIM) framework [9], is devised. Most of the aforementioned approaches typically employ a grid of possible values for the angle of arrival (AOA), where each of them is representative of a specific angular bin. However, in many situations, grid selection is a challenging task that in general leads to a mismatched signal model with subsequent estimation errors [11].

Unlike methods that depend on a fixed set of nominal AOAs, the approach in this paper offers flexibility by adjusting the atoms so as to accommodate angle displacements. In this regard, the recovery process of the angle-frequency profile is framed as a regularized maximum likelihood (RML) estimation, aimed at exploiting the inherent block-sparsity of the entire profile. The resulting optimization problem is tackled using a minorization-maximization (MM)-maximum block improvement (MBI) paradigm. This method iteratively refines the estimates of three block variables, viz., noise power, 2-D profile, and angular displacements. Specifically, by dynamically focusing on each block, the MBI improves the accuracy of the angle-frequency profile recovery process. To further boost the reliability of the space-frequency occupancy map determination and reduce the angular displacements estimation error, two refinement strategies for the 2-D spectrum inference are adopted. In the former, the Bayesian information criterion (BIC) is exploited to obtain a bespoke selection of the dominant atoms. In the latter, a two-stage approach (involving the orthogonal matching pursuit (OMP) algorithm [12] and the false discovery rate (FDR) paradigm [13]) for selecting the most relevant contributions is adopted. Interesting case studies are provided to validate the proposed framework.

II. System and signal model

Let us consider a radar system exploiting a uniform linear array (ULA) of M antenna elements, that collects the signals transmitted by K sources located at specific unknown angular directions, say $\bar{\theta}_1, \ldots, \bar{\theta}_K$, each with its own (unknown) bandwidth. Let us also assume that there is only one source arriving from a specific angular direction. The baseband discrete-time signal at the output of the receiving array for the h-th snapshot,

The work of Augusto Aubry and Antonio De Maio was in part supported by the European Union under the Italian National Recovery and Resilience Plan (NRRP) of NextGenerationEU, partnership on "Telecommunications of the Future" (PE00000001 - Program "RESTART"), and in part by the European Union in the NextGenerationEU plan through the Italian program "Bando PRIN 2022," D.D. 104/2022 (PE7, project "CIRCE," code E53D23000410006).

$h = 1, \ldots, N_1$, with N_1 the total number of available data-windows, can be written as

$$\boldsymbol{y}_h = \sum_{k=1}^{K} \sum_{m=1}^{N_F} \bar{\boldsymbol{s}}(\bar{\theta}_k, \omega_m) \bar{a}_{k,m,h} + \boldsymbol{w}_h, \tag{1}$$

where $N_F \geq N$ is the number of frequency bins, with N the number of available temporal observations per snapshot, $\boldsymbol{w}_1, \ldots, \boldsymbol{w}_{N_1} \in \mathbb{C}^{NM}$ are the disturbance vectors affecting the different data-windows, modeled as independent and identically distributed zero-mean circularly symmetric white Gaussian vectors, with mean square value σ^2, and $\bar{a}_{k,m,h}$ is a scalar term proportional to the Fourier transform of the signal samples emitted by the k-th source (during the h-th data window) at the normalized frequency $\omega_m = (m-1)/N_F$, $m = 1, \ldots, N_F$. Moreover, $\bar{\boldsymbol{s}}(\theta, \omega)$ is the space-frequency steering vector associated with the angle θ and the frequency ω, i.e.,

$$\bar{\boldsymbol{s}}(\theta, \omega) = \boldsymbol{s}_F(\omega) \otimes \boldsymbol{s}(\theta), \tag{2}$$

with $\boldsymbol{s}_F(\omega)$ and $\boldsymbol{s}(\theta)$, the frequency and spatial steering vector, respectively, while $\otimes$ denotes the Kronecker product.

To proceed further, let us introduce a grid of L angular locations θ_i, $i = 1, \ldots, L$, chosen sufficiently dense such that there will be at most one source within each bin $[\theta_i - \delta/2, \theta_i + \delta/2]$, having indicated with δ the discretization step. Differently from [10], the actual source angle of arrival (AOA) is modeled as the closest grid point plus a displacement, i.e., $\bar{\theta}_i = \theta_i + \Delta\theta_i$, $i = 1, \ldots, L$. Hence, the signal model (1), can be expressed in the following form

$$\boldsymbol{y}_h = \sum_{i=1}^{L} \sum_{m=1}^{N_F} \bar{\boldsymbol{s}}(\theta_i + \Delta\theta_i, \omega_m) a_{i,m,h} + \boldsymbol{w}_h, \tag{3}$$

where $\bar{\boldsymbol{s}}(\theta_i + \Delta\theta_i, \omega_m)$, $i = 1, \ldots, L$, $m = 1, \ldots, N_F$, define the overall dictionary and $a_{i,m,h}$, $i = 1, \ldots, L$, $m = 1, \ldots, N_F$, represent the unknown space-frequency profile at the h-th snapshot.

Let us now assume δ small enough such that the displacement effect on the actual steering vector in each bin can be modeled resorting to the first-order Taylor expansion of $\bar{\boldsymbol{s}}(\theta_i + \Delta\theta_i, \omega_m)$ around θ_i, i.e., [11], [14]

$$\bar{\boldsymbol{s}}(\theta_i + \Delta\theta_i, \omega_m) \simeq \bar{\boldsymbol{s}}(\theta_i, \omega_m) + \dot{\boldsymbol{s}}(\theta_i, \omega_m)\Delta\theta_i, \; i = 1, \ldots, L, \tag{4}$$

with $\dot{\boldsymbol{s}}(\theta_i, \cdot)$ the derivative of $\bar{\boldsymbol{s}}(\theta_i, \cdot)$ with respect to θ evaluated at $\theta = \theta_i$, whose expression is provided in [15].

According to (4), the signal model in (3) boils down to

$$\boldsymbol{y}_h = \boldsymbol{H}\left(\boldsymbol{\Delta\theta}\right) \boldsymbol{x}_h + \boldsymbol{w}_h, \; h = 1, \ldots, N_1 \tag{5}$$

where $\boldsymbol{x}_h = [a_{1,1,h}, \ldots, a_{1,N_F,h}, a_{2,1,h}, \ldots, a_{L,N_F,h}]^T \in \mathbb{C}^{LN_F}$ is the vector containing the space-frequency profile for the h-th snapshot, whereas the matrix $\boldsymbol{H}(\cdot) \in \mathbb{C}^{NM \times LN_F}$ corresponds to the model matrix given by

$$\begin{aligned}\boldsymbol{H}\left(\boldsymbol{\Delta\theta}\right) = \\ &[\bar{\boldsymbol{s}}(\theta_1, \omega_1) + \dot{\boldsymbol{s}}(\theta_1, \omega_1)\Delta\theta_1, \ldots, \bar{\boldsymbol{s}}(\theta_1, \omega_{N_F}) + \dot{\boldsymbol{s}}(\theta_1, \omega_{N_F})\Delta\theta_1, \\ &\bar{\boldsymbol{s}}(\theta_2, \omega_1) + \dot{\boldsymbol{s}}(\theta_2, \omega_1)\Delta\theta_2, \ldots, \bar{\boldsymbol{s}}(\theta_L, \omega_{N_F}) + \dot{\boldsymbol{s}}(\theta_L, \omega_{N_F})\Delta\theta_L],\end{aligned} \tag{6}$$

with $\boldsymbol{\Delta\theta} = [\Delta\theta_1, \ldots, \Delta\theta_L]^T$.

The overall measurements collected at the receiver can be compactly written as

$$\boldsymbol{Y} = \boldsymbol{H}\left(\boldsymbol{\Delta\theta}\right) \boldsymbol{X} + \boldsymbol{W}, \tag{7}$$

with

$$\boldsymbol{Y} = [\boldsymbol{y}_1, \ldots, \boldsymbol{y}_{N_1}] \in \mathbb{C}^{MN \times N_1},$$

$$\boldsymbol{X} = \begin{bmatrix} \boldsymbol{x}_1 \\ \vdots \\ \boldsymbol{x}_{LN_F} \end{bmatrix} = [\boldsymbol{x}^1, \ldots, \boldsymbol{x}^{N_1}] \in \mathbb{C}^{LN_F \times N_1},$$

and

$$\boldsymbol{W} = [\boldsymbol{w}_1, \ldots, \boldsymbol{w}_{N_1}] \in \mathbb{C}^{MN \times N_1}.$$

III. Problem formulation and estimation procedure

In this section, a space-frequency profile recovery framework leveraging on the MM-MBI paradigm is introduced. In particular, it can be obtained as the solution to the following RML estimation problem

$$\mathcal{P} \begin{cases} \min\limits_{\boldsymbol{X}, \sigma^2, \boldsymbol{\Delta\theta}} & NMN_1 \log(\sigma^2) \\ & + \frac{1}{\sigma^2} \|\boldsymbol{H}(\boldsymbol{\Delta\theta})\boldsymbol{X} - \boldsymbol{Y}\|^2 + f_1(\boldsymbol{X}) \\ \text{s.t.} & \sigma_L^2 \leq \sigma^2 \leq \sigma_U^2 \\ & |\Delta\theta_i| \leq \delta/2, \; i = 1, \ldots, L, \end{cases} \tag{8}$$

where $\|\cdot\|$ denotes the Frobenius matrix norm, and

$$f_1(\boldsymbol{X}) = \sum_{k=1}^{LN_F} \frac{2}{q} \left[\left(\|\boldsymbol{x}_k\|^2 + \epsilon \right)^{q/2} - 1 \right] \tag{9}$$

is the block-sparsity promoting penalty term, while σ_L^2 and σ_U^2 are a lower bound and an upper bound to the noise power level, respectively. Moreover, $\epsilon > 0$ is a smoothing factor making (9) differentiable, whereas the parameter $0 < q \leq 1$ rules the l_q-norm of the vector containing the space-frequency source energies.

Problem $\mathcal{P}$ is a non-convex and in general non-polynomial (NP)-hard optimization problem. Nevertheless, a high quality solution can be obtained resorting to the MM-MBI paradigm [16], [17], where the noise variance σ^2, the space-frequency profile $\boldsymbol{X}$, and the off-grid angle displacements $\boldsymbol{\Delta\theta}$ are considered as variable blocks. In the MM-MBI framework, the optimization vector is first split into blocks of disjoint variables and the objective function (or its surrogate) is minimized with respect to each block while keeping unaltered the others. Hence, only the block ensuring the best result in terms of objective function is updated for the next iteration step. In other words, at each iteration, the MBI updates only the variable block providing the best objective improvement, while keeping the others settled to their previous values.

To proceed formally with reference to Problem $\mathcal{P}$, let us introduce the optimization variables, $\mathcal{Y} = \left\{\sigma^2, \boldsymbol{X}, \boldsymbol{\Delta\theta}\right\}$, which are partitioned into three blocks. Hence, $\mathcal{Y}^{(n-1)}$ denotes the optimized variables at the $(n-1)$-th iteration, that is

$$\mathcal{Y}^{(n-1)} = \left\{ \sigma^{2(n-1)}, \boldsymbol{X}^{(n-1)}, \boldsymbol{\Delta\theta}^{(n-1)} \right\}. \tag{10}$$

Then, the MM-MBI procedure requires solving three subproblems at each iteration to update the optimized solution [16], [17]. In particular, the solution to the subproblems concerning either the variables σ^2 or $\boldsymbol{X}$ can be obtained in closed form using a procedure similar to that in [10] (see steps 5 and 6 of Algorithm 1).

An optimal solution $\boldsymbol{\Delta\theta}$, where $\boldsymbol{X}$ and σ^2 are fixed, can be derived leveraging the MBI approach with respect to the set of variables $\{\Delta\theta_1, \dots, \Delta\theta_L\}$ to Problem (8) restricted to $\boldsymbol{\Delta\theta}$. In this respect, let us denote by $\mathcal{Y}_1^{(n_1-1)} = \left\{\Delta\theta_1^{(n_1-1)}, \Delta\theta_2^{(n_1-1)}, \dots, \Delta\theta_L^{(n_1-1)}\right\}$, i.e., the optimized variables at the (n_1-1)-th inner iteration.

Then, the MBI approach requires solving the following L subproblems at each iteration [18], namely

$$\mathcal{P}_3^i \begin{cases} \min\limits_{\Delta\theta_i} & \left\| \boldsymbol{H}(\widetilde{\boldsymbol{\Delta\theta}}_i)\boldsymbol{X} - \boldsymbol{Y} \right\|^2 \\ \text{s.t.} & |\Delta\theta_i| \leq \delta/2 \end{cases} \tag{11}$$

for $i = 1, \dots, L$, where

$$\widetilde{\boldsymbol{\Delta\theta}}_i = \left[\Delta\theta_1^{(n_1-1)}, \dots, \Delta\theta_{i-1}^{(n_1-1)}, \Delta\theta_i, \Delta\theta_{i+1}^{(n_1-1)}, \dots, \Delta\theta_L^{(n_1-1)}\right]^T. \tag{12}$$

It can be shown that the closed-form solution to Problem $\mathcal{P}_3^i$, for a fixed i, is given by

$$\Delta\theta_i = \min\left(\frac{\delta}{2}, \max\left(-\frac{\delta}{2}, \frac{\text{Re}\left[\boldsymbol{c}_i{}^\dagger\left(\boldsymbol{\zeta} - \boldsymbol{C}_{-i}\boldsymbol{\Delta\theta}_{-i}\right)\right]}{\|\boldsymbol{c}_i\|^2}\right)\right), \tag{13}$$

with Re$\{\cdot\}$ the real-part of a complex number, $(\cdot)^\dagger$ the conjugate transpose operator, and $\boldsymbol{C}_{-i} \in \mathbb{C}^{MNN_1\times(L-1)}$ the matrix obtained from $\boldsymbol{C} = [\boldsymbol{c}_1, \dots, \boldsymbol{c}_L] \in \mathbb{C}^{MNN_1\times L}$ removing its i-th column, where

$$\boldsymbol{c}_i = \sum_{k=1}^{N_F} \boldsymbol{B}_{(i-1)N_F+k}, \quad \boldsymbol{B} = \begin{bmatrix} \dot{\boldsymbol{H}}\textbf{diag}\left(\boldsymbol{x}^1\right) \\ \vdots \\ \dot{\boldsymbol{H}}\textbf{diag}\left(\boldsymbol{x}^{N_1}\right) \end{bmatrix}, \tag{14}$$

$\boldsymbol{\Delta\theta}_{-i} \in \mathbb{C}^{(L-1)\times 1}$ the vector containing all the entries of $\boldsymbol{\Delta\theta}$ except that in position i, and

$$\boldsymbol{\zeta} = \begin{bmatrix} \boldsymbol{z}^1 \\ \vdots \\ \boldsymbol{z}^{N_1} \end{bmatrix}, \quad \text{with} \quad \boldsymbol{Z} = [\boldsymbol{z}^1, \dots, \boldsymbol{z}^{N_1}] = \boldsymbol{Y} - \bar{\boldsymbol{H}}\boldsymbol{X}. \tag{15}$$

Here, $\bar{\boldsymbol{H}}$ and $\dot{\boldsymbol{H}}$ are the matrices whose columns are respectively $\bar{\boldsymbol{s}}(\theta_i, \omega_m)$ and $\dot{\boldsymbol{s}}(\theta_i, \omega_m)$, $i = 1, \dots, L$, $m = 1, \dots, N_F$.

The MM-MBI based procedure developed in this paper for off-grid 2-D spectrum sensing is summarized in Algorithm 1. Note that the procedure in Algorithm 1 is executed until convergence (or a maximum number of iterations n_{max}) is reached, i.e., $g(\mathcal{Y}^{(n-1)}) - g(\mathcal{Y}^{(n)}) < \xi$ or $n = n_{max}$, with $g(\mathcal{Y}^{(n)}) = NMN_1 \log(\sigma^{2(n)}) + \frac{1}{\sigma^{2(n)}}\left\|\boldsymbol{H}(\boldsymbol{\Delta\theta}^{(n)})\boldsymbol{X}^{(n)} - \boldsymbol{Y}\right\|^2 + f_1(\boldsymbol{X}^{(n)})$.

Algorithm 1 MM-MBI based strategy

1: **Input.** σ_L^2, σ_U^2, ϵ, $\boldsymbol{H}$, $\boldsymbol{Y}$, $\boldsymbol{X}^{(0)}$, ξ, n_{max}, δ, and $q \in [0, 1]$.

2: **Initialization.** Set $n = 0$, $\boldsymbol{\Delta}\theta^{(0)} = \boldsymbol{0}$, and $\sigma^{2(0)} = \min\left(\max\left(\sigma_L^2, \hat{\sigma}^2\right), \sigma_U^2\right)$.

3: **repeat**

4: $n = n + 1$.

5: Compute $\sigma^{2(n)} = \min\left(\max\left(\sigma_L^2, \hat{\sigma}^2\right), \sigma_U^2\right)$, and evaluate the resulting objective $\nu_1^{(n)}$, where

$$\hat{\sigma}^2 = \frac{1}{NMN_1}\|\boldsymbol{H}(\boldsymbol{\Delta\theta}^{(n-1)})\boldsymbol{X}^{(n-1)} - \boldsymbol{Y}\|^2.$$

6: Compute

$$\boldsymbol{X}^{(n)} = \boldsymbol{D}_{\boldsymbol{X}^{(n-1)}}^{-2}\boldsymbol{H}^\dagger(\boldsymbol{\Delta\theta}^{(n-1)}) \left(\boldsymbol{H}(\boldsymbol{\Delta\theta}^{(n-1)})\boldsymbol{D}_{\boldsymbol{X}^{(n-1)}}^{-2}\boldsymbol{H}^\dagger(\boldsymbol{\Delta\theta}^{(n-1)}) + \sigma^{2(n-1)}\boldsymbol{I}\right)^{-1}\boldsymbol{Y}$$

where

$$\boldsymbol{D}_{\boldsymbol{X}^{(n-1)}} = \textbf{diag}\left(\frac{1}{\left(\|\boldsymbol{X}_1^{(n-1)}\|^2 + \epsilon\right)^{\frac{1}{2}-\frac{q}{4}}}, \dots, \frac{1}{\left(\|\boldsymbol{X}_{LN_F}^{(n-1)}\|^2 + \epsilon\right)^{\frac{1}{2}-\frac{q}{4}}}\right),$$

and evaluate the resulting objective $\nu_2^{(n)}$.

7: Compute $\boldsymbol{\Delta\theta}^{(n)}$, via the inner MBI based technique, and evaluate the resulting objective $\nu_3^{(n)}$.

8: Select $k^\star = \arg\min\limits_{k=1,\dots,3} \nu_k^{(n)}$, and update the block $k^\star$ in $\mathcal{Y}^{(n-1)}$.

9: **until** $g(\mathcal{Y}^{(n-1)}) - g(\mathcal{Y}^{(n)}) \geq \xi$ or $n < n_{max}$

10: **Output.** $\hat{\sigma}^2 = \sigma^{2(n)}$, $\hat{\boldsymbol{X}} = \boldsymbol{X}^{(n)}$, and $\widehat{\boldsymbol{\Delta\theta}} = \boldsymbol{\Delta\theta}^{(n)}$.

IV. 2-D Spectrum Profile Estimate Refinement Strategies

Leveraging the output provided by Algorithm 1, in this section, effective procedures for refining the 2-D spectrum profile estimated using the RML framework are now proposed. Each refinement technique follows the guidelines outlined below:

- The vector containing the displacement estimates at the output of Algorithm 1, $\widehat{\boldsymbol{\Delta\theta}}$, is used to construct the new updated dictionary. Precisely, the complete model matrix $\mathring{\boldsymbol{H}}(\widehat{\boldsymbol{\Delta\theta}})$ is constructed (leveraging (2)), which represents the learned dictionary obtained from Algorithm 1.
- Identification of the active atoms in $\mathring{\boldsymbol{H}}(\widehat{\boldsymbol{\Delta\theta}})$ via model selection rules aimed at providing an estimate $\mathcal{R}$ of the sources support, and definition of the resulting source subspace $\hat{\boldsymbol{H}}(\widehat{\boldsymbol{\Delta\theta}})$.
- Estimation of the 2-D space-frequency profile $\tilde{\boldsymbol{X}}$ resorting to the least squares (LS) paradigm to infer the behavior of the of $\hat{\boldsymbol{X}}$ corresponding to the active atoms, i.e., the columns of $\hat{\boldsymbol{H}}(\widehat{\boldsymbol{\Delta\theta}})$.
- Update of the angle displacement estimates executing the inner MBI algorithm with $\tilde{\boldsymbol{X}}$ and $\hat{\boldsymbol{H}}(\widehat{\boldsymbol{\Delta\theta}})$ as inputs.

Two approaches for the selection of the active atoms are considered. The first method relies on an extension of the on-grid method proposed in [10], and is referred to as off-grid MM-MBI BIC based 2-D spectrum sensing (OG-MBI-BIC), not reported here for sake of brevity. The second technique leverages a two-stage procedure, comprising a coarse and a fine screening. The former faces with the selection of at most κ columns of $\mathring{\boldsymbol{H}}(\widehat{\boldsymbol{\Delta\theta}})$ that likely span the useful signal subspace, leading to the matrix $\breve{\boldsymbol{H}}(\widehat{\boldsymbol{\Delta\theta}})$. The latter eventually establishes the actual active atoms by applying the FDR algorithm of in [13].

As to the second phase, starting from the dominant atoms collected in $\breve{\boldsymbol{H}}(\widehat{\boldsymbol{\Delta\theta}})$, the LS estimate of $\boldsymbol{X}$ is computed as

$$\breve{\boldsymbol{X}} = \left(\breve{\boldsymbol{H}}^{\dagger}(\widehat{\boldsymbol{\Delta\theta}})\breve{\boldsymbol{H}}(\widehat{\boldsymbol{\Delta\theta}})\right)^{-1}\breve{\boldsymbol{H}}^{\dagger}(\widehat{\boldsymbol{\Delta\theta}})\boldsymbol{Y}, \tag{16}$$

and its approximate error covariance matrix estimate is evaluated as

$$\hat{\boldsymbol{\Sigma}} = \frac{1}{NMN_1}\left\|\boldsymbol{Y} - \breve{\boldsymbol{H}}(\widehat{\boldsymbol{\Delta\theta}})\breve{\boldsymbol{X}}\right\|^2\left(\breve{\boldsymbol{H}}^{\dagger}(\widehat{\boldsymbol{\Delta\theta}})\breve{\boldsymbol{H}}(\widehat{\boldsymbol{\Delta\theta}})\right)^{-1}. \tag{17}$$

Therefore, the problem of estimating $\mathcal{R}$ can be viewed as testing the following κ null hypotheses

$$\begin{cases} H_1 & : & \breve{\boldsymbol{x}}_1 = 0 \\ \vdots & : & \vdots \\ H_\kappa & : & \breve{\boldsymbol{x}}_\kappa = 0 \end{cases}. \tag{18}$$

In this regard, the test statistics

$$T_k \triangleq \frac{\|\breve{\boldsymbol{x}}_k\|^2}{\hat{\boldsymbol{\Sigma}}(k,k)}, \tag{19}$$

are employed, where $\hat{\boldsymbol{\Sigma}}(k,k)$ is the (k,k)-th entry of $\hat{\boldsymbol{\Sigma}}$. Under null hypotheses, T_k can be approximated with a $\chi^2_{N_1}$ random variable. Now, the FDR algorithm can be implemented as summarized in Algorithm 2. Finally, the dictionary matrix screened by the FDR, $\hat{\boldsymbol{H}}(\widehat{\boldsymbol{\Delta\theta}})$, is used to recover the 2-D profile containing only the effective atoms, i.e., $\tilde{\boldsymbol{X}}$.

Let us now focus on the coarse screening stage, which is accomplished by employing the OMP [12], herein described with respect to its extension to the row-sparsity case. It is a regressor selection algorithm which preselects a number κ of regressors and obtains the LS estimates of the corresponding coefficients. Being it an iterative greedy selection process, at each iteration, it determines the most dominant regressors from the available set [12]. The main steps involved in the OMP technique are summarized in Algorithm 3, where κ denotes an upper-bound to the number of dominant atoms, $\mathring{\boldsymbol{h}}_k$ is the k-th column of the matrix $\mathring{\boldsymbol{H}}(\widehat{\boldsymbol{\Delta\theta}})$, and $\mathcal{R}^i = \{r(1), \ldots, r(i)\}$ indicates the space-frequency support estimate up to the i-th iteration. Hence, the model matrix at the output of the OMP is given by $\breve{\boldsymbol{H}}(\widehat{\boldsymbol{\Delta\theta}}) = \mathring{\boldsymbol{H}}_{\mathcal{R}^\kappa}$.

Algorithm 1 along with the OMP-FDR based refinement is indicated as off-grid MM-MBI OMP-FDR based 2-D spectrum sensing (OG-MBI-OFDR).

Algorithm 2 FDR for 2-D Spectrum Sensing

Input. $\breve{\boldsymbol{H}}$ and $\boldsymbol{Y}$.
Compute the LS estimate of $\boldsymbol{X}$ as in (16) and $\hat{\boldsymbol{\Sigma}}$ as in (17).
Compute the test statistics T_k, $k = 1, \ldots, \kappa$ using (19).
Sort T_k, $k = 1, \ldots, \kappa$, in decreasing order, viz., $T_{[1]} \geq \ldots \geq T_{[\kappa]}$.
Compute the l-th probability P_l as $P_l = \frac{\alpha\, l}{\kappa \eta_\kappa}$, $l = 1, \ldots, \kappa$, with $\eta_\kappa = \log(\kappa) + 0.577$ and α the false discovery rate.
Compute the l-th threshold from a $\chi^2_{N_1}$ distribution with N_1 degrees of freedom as

$$\omega_{P_l} : \text{Prob}\left[T_{[l]} \geq \omega_{P_l} | H_{[l]}\right] = P_l$$

Find $\hat{l} \triangleq \max\left[l : T_{[i]} \geq \omega_{P_i}, i = 1, \ldots, l\right]$
Reject the null hypotheses $H_{[i]}$ for $i = 1, \ldots, \hat{l}$ and accept $H_{[\hat{l}+1]}, \ldots, H_{[\kappa]}$
Estimate the support as $\mathcal{R}_{FDR} = \left\{[1], [2], \ldots, [\hat{l}]\right\}$.
Output. $\hat{\boldsymbol{H}}(\widehat{\boldsymbol{\Delta\theta}}) = \breve{\boldsymbol{H}}_{\mathcal{R}_{FDR}}$.

Algorithm 3 OMP for 2-D spectrum sensing

Input. $\mathring{\boldsymbol{H}}$, $\boldsymbol{Y}$, and κ.
Initialization. Set $\boldsymbol{R}_0 = \boldsymbol{Y}$, and $\mathcal{R}^0 = \emptyset$.
for $i = 1 : \kappa$. **do**
    $k_i = \arg\max_{k \in [1, \ldots, LN_F] - \mathcal{R}^{i-1}} \|\mathring{\boldsymbol{h}}_k^{\dagger}\boldsymbol{R}_{i-1}\|^2$
    $\mathcal{R}^i = \mathcal{R}^{i-1} \cup k_i$
    $\boldsymbol{R}_i = \left(\boldsymbol{I} - \mathring{\boldsymbol{H}}_{\mathcal{R}^i}\left(\mathring{\boldsymbol{H}}^{\dagger}_{\mathcal{R}^i}\mathring{\boldsymbol{H}}_{\mathcal{R}^i}\right)^{-1}\mathring{\boldsymbol{H}}^{\dagger}_{\mathcal{R}^i}\right)\boldsymbol{Y}$
end for
Output. $\breve{\boldsymbol{H}}(\widehat{\boldsymbol{\Delta\theta}}) = \mathring{\boldsymbol{H}}_{\mathcal{R}^\kappa} \in \mathbb{C}^{NM \times \kappa}$.

V. Performance assessment

The purpose of this section is to assess the effectiveness of the proposed framework in terms of 2-D spectrum sensing capabilities. To this end, the two approaches OG-MBI-BIC, and OG-MBI-FDR are compared with the procedure devised in [10] (shortly indicated as BIC-BSLIM), that is also used to initialize the two algorithms. Additionally, the gridless method in [19] designed for 2D DOA estimation (denoted as 2D-MNOMP in the following) is also used as term of comparison.

The considered system comprises a ULA with $M = 10$ equally spaced antennas (with inter-element distance of $\lambda_0/2$, i.e., half wavelength), operating at frequency $f_0 = 2.4$ GHz, with a bandwidth of $B = 500$ MHz. The analyzed scenario assumes $K = 4$ emitters with their AOAs described by $\bar{\theta}_k = \{0°, 18°, 36°, -18°\}$ and $\Delta\theta_k = \{0.643°, 1.125°, 0.750°, 0.900°\}$, $k = 1, \ldots, 4$. Moreover, the first three emitters are communication sources operating on $[-0.1B - \frac{1}{2T_s}(1+\beta), -0.1B + \frac{1}{2T_s}(1+\beta)]$, $[0.2B - \frac{1}{2T_s}(1+\beta), 0.2B + \frac{1}{2T_s}(1+\beta)]$, and $[-\frac{1}{2T_s}(1+\beta), \frac{1}{2T_s}(1+\beta)]$, respectively, with $\beta = 0.5$ and $T_s = 10/B$. The fourth emitter is a jammer radiating a zero-mean circularly symmetric Gaussian signal with a flat spectrum over $[-0.1B, 0.1B]$.

Finally, $\sigma^2 = 0$ dB and two case studies are assessed: the former entails a signal to noise ratio (SNR) of 5 dB for all the emitters, the latter supposes SNR $= 10$ dB still for all the sources.

The discretization grid is realized with $L = 40$ uniformly spaced angles over the interval $[-90°, 90°[$, corresponding to a step $\delta = 4.5°$. As to the available temporal observations, $N_1 = 10$ independent data-windows are processed each with $N = 50$ temporal observations and $N_F = 2N$. Regarding the parameter settings employed by Algorithm 1, they are set as $\xi = 10^{-1}$, $n_{max} = 30$, $\epsilon = 10^{-6}$, $q = 0.6$. The same exit condition is applied for the inner MBI algorithm. Moreover, the OG-MBI-OFDR approach assumes $\alpha = 0.05$ and $\kappa = 40$, whereas $\bar{K} = 180$ is adopted in OG-MBI-BIC. Regarding the 2D-MNOMP, its parameters are set as follows: oversampling factors equal to $(4, 4)$, and model order overestimating probability set as $P_{oe} = 10^{-4}$. Moreover, being the noise power σ^2 an unknown parameter (its true value is 0 dB), and only an estimate $\hat{\sigma}^2$ is reasonably available, the tests are conducted assuming either an ideal matched case $\hat{\sigma}^2 = 0$ dB, or a mismatched situation due to the unavoidable estimation errors, i.e., $\hat{\sigma}^2 = -3$ dB.

Figure 1(a) displays the nominal space-frequency profile of the aforementioned simulation scenario with SNR $= 10$ dB, obtained by evaluating for each angle bin the average (over the N_1 data-windows) Energy Spectral Density (ESD) of the signal received on the AOA of the associated emitter, normalized to the maximum value. The plot clearly demonstrates the space-frequency regions occupied by the four emitters. In subplots (b)-(f) of Figure 1, the results of the space-frequency occupancy maps recovery process provided by OG-MBI-BIC, OG-MBI-OFDR, BIC-BSLIM, 2D-MNOMP with $\hat{\sigma}^2 = 0$ dB, and 2D-MNOMP with $\hat{\sigma}^2 = -3$ dB are illustrated, with reference to one simulation trial.

From a visual comparison of the reconstructed 2-D maps with the ground-truth, it is evident that the OG-MBI-BIC, OG-MBI-OFDR, and 2D-MNOMP (with a perfect noise power knowledge) techniques can provide an almost perfect recovery, accurately localizing the sources in both the angle and frequency domains. Regarding the 2D-MNOMP, the results show that in the presence of the unavoidable estimation error in the noise power the false alarms increase. Notably, the proposed off-grid recovery strategies localize all four sources within the correct spatial bins, without generating false alarms in other angular directions. On the other hand, BIC-BSLIM [10], which does not account for off-grid behavior, introduces model mismatches that result in false alarms at other AOAs that represent ghost sources. Noteworthy, all approaches detect only a subset of the frequency bins per emitter, yielding maps with an on-off pattern. This behavior can be attributed to the dictionary redundancy in the frequency domain and sparsity promoting nature of the developed methods.

To provide further insights, the performance of the different strategies across multiple trials is analyzed. Specifically, the empirical false alarm rate, P_{fa}, and the empirical detection probability, P_d, are used as performance metrics. These are

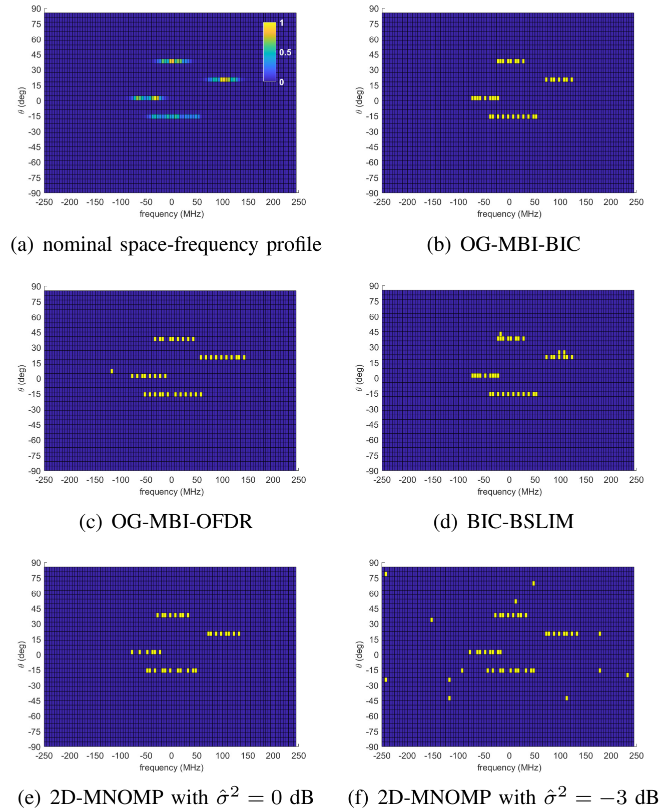

(a) nominal space-frequency profile (b) OG-MBI-BIC

(c) OG-MBI-OFDR (d) BIC-BSLIM

(e) 2D-MNOMP with $\hat{\sigma}^2 = 0$ dB (f) 2D-MNOMP with $\hat{\sigma}^2 = -3$ dB

Fig. 1. Space-frequency occupancy map for the analyzed scenario with SNR $= 10$ dB. Subplots refer to a) nominal space-frequency profile, b) OG-MBI-BIC, c) OG-MBI-OFDR, d) BIC-BSLIM, e) 2D-MNOMP with $\hat{\sigma}^2 = 0$ dB, and f) 2D-MNOMP with $\hat{\sigma}^2 = -3$ dB.

computed by counting the number of detections within source-free and source-occupied space-frequency bins, respectively. To account for the inherent on-off behavior observed in the recovered maps, a moving average filter (with two equal weights) is applied along the frequency dimension of the recovered profiles for all considered techniques.

In Table I the empirical false alarm rate and detection probability are reported for the simulation setup illustrated in Figure 1(a) and for two different SNR values, viz., SNR $= 5$ dB and SNR $= 10$ dB. Moreover, both P_{fa} and P_d are evaluated over 10 independent trials, where at each run there are $N_1 = 10$ independent data-windows, corresponding to 39370 emitters free space-frequency bins and 630 bins occupied by RF sources. The results clearly show that both the OG-MBI-BIC and the OG-MBI-OFDR achieve high P_d values. Notably, the OG-MBI-OFDR exhibits the best detection performance, being able to ensure $P_d = 0.98$ also at low SNRs. However, this advantage comes at the cost of higher computational complexity. Moreover, the OG-MBI-BIC ensures lower P_{fa} values than the OG-MBI-OFDR, since the OG-MBI-OFDR tends to provide an enlarged frequency support for each emitter. Finally, it is not surprising that the BIC-BSLIM is also capable of ensuring high detection performance, although it introduces false alarms in directions adjacent to those of the true sources, thereby resulting in ghost sources estimation.

TABLE I
EMPIRICAL FALSE ALARM RATE AND DETECTION PROBABILITY.

	SNR = 5 dB		SNR = 10 dB	
	P_{fa}	P_d	P_{fa}	P_d
OG-MBI-BIC	~ 0	0.56	2.0×10^{-4}	0.94
OG-MBI-OFDR	28×10^{-4}	0.98	13×10^{-4}	0.98
BIC-BSLIM	~ 0	0.55	8.2×10^{-4}	0.94
2D-MNOMP with $\hat{\sigma}^2 = -3$ dB	115×10^{-4}	0.89	101×10^{-4}	0.94
2D-MNOMP with $\hat{\sigma}^2 = 0$ dB	1×10^{-4}	0.83	1.3×10^{-4}	0.91

To quantitatively measure the accuracy of the AOA estimation of the proposed strategies, the root mean square error (RMSE) of the angle displacements is also evaluated. To this end, the focus is only on the bins occupied by the sources. In order to proceed, let $\widehat{\boldsymbol{\Delta\theta}}_r$ be the vector containing the displacement estimates associated with the source directions and let $\boldsymbol{\Delta\theta}_r$ be the vector whose entries are the corresponding true displacements. The RMSE (constrained to the actual source angle bins) is thus defined as

$$\text{RMSE} = \sqrt{\mathbb{E}\left[\left\|\widehat{\boldsymbol{\Delta\theta}}_r - \boldsymbol{\Delta\theta}_r\right\|^2\right]}. \tag{20}$$

Since a closed-form expression for the RMSE in (20) is not available, the Monte Carlo simulation strategy is used for its computation. The results are reported in Table II, which show that the various space-frequency recovery procedures are capable of accurately estimating the source AOA, i.e., effectively learning the actual model dictionary. It is not surprising that both the proposed algorithms yield approximately the same RMSE, outperforming the on-grid counterpart, which indeed does not account for possible displacements within the considered grid.

TABLE II
RMSE OF ANGULAR DISPLACEMENT.

	SNR = 5 dB	SNR = 10 dB
OG-MBI-BIC	0.34 deg	0.31 deg
OG-MBI-OFDR	0.37 deg	0.32 deg
BIC-BSLIM	1.75 deg	1.75 deg
2D-MNOMP with $\hat{\sigma}^2 = -3$ dB	0.73 deg	0.56 deg
2D-MNOMP with $\hat{\sigma}^2 = 0$ dB	0.31 deg	0.18 deg

VI. CONCLUSIONS

This paper addressed the problem of off-grid 2-D spectrum sensing for cognitive radars. An off-grid 2-D profile recovery strategy using RML estimation is proposed, leveraging the block-sparsity of the profile. The inference problem is handled through an MM-MBI approach, dynamically estimating noise power, 2-D profile, and angular displacements. To enhance the reliability and accuracy of the space-frequency occupancy map and AOA estimates, two refinement procedures were introduced to suitably select dominant active atoms in the profile. Numerical simulations validated the effectiveness of the framework, with the BIC-based refinement achieving the best trade-off between computational complexity and estimation accuracy. As future research avenues, it would be worthwhile to extend the approach to account for both azimuth and elevation angles, as well as testing the algorithms on measured data.

REFERENCES

[1] S. Haykin, "Cognitive Radar: A Way of the Future," *IEEE Signal Processing Magazine*, vol. 23, no. 1, pp. 30–40, 2006.

[2] A. Farina, A. De Maio, and S. Haykin, "The Impact of Cognition on Radar Technology," Scitech Publishing, Rijeka, Croatia, Tech. Rep., 2017.

[3] M. Wicks, "Spectrum Crowding and Cognitive Radar," in *2nd International Workshop on Cognitive Information Processing*. IEEE, 2010, pp. 452–457.

[4] A. Aubry, V. Carotenuto, A. De Maio, A. Farina, and L. Pallotta, "Optimization Theory-Based Radar Waveform Design for Spectrally Dense Environments," *IEEE Aerospace and Electronic Systems Magazine*, vol. 31, no. 12, pp. 14–25, 2016.

[5] H. Tang, "Some Physical Layer Issues of Wide-Band Cognitive Radio Systems," in *First IEEE International Symposium on New Frontiers in Dynamic Spectrum Access Networks (DySPAN)*. IEEE, 2005, pp. 151–159.

[6] A. Fehske, J. Gaeddert, and J. Reed, "A New Approach to Signal Classification using Spectral Correlation and Neural networks," in *First IEEE International Symposium on New Frontiers in Dynamic Spectrum Access Networks (DySPAN)*. Baltimore, MD, USA: IEEE, 2005, pp. 144–150.

[7] K.-L. Du and W. H. Mow, "Affordable Cyclostationarity-Based Spectrum Sensing for Cognitive Radio With Smart Antennas," *IEEE Transactions on Vehicular Technology*, vol. 59, no. 4, pp. 1877–1886, 2010.

[8] D. A. Guimaraes, R. A. A. de Souza, and A. N. Barreto, "Performance of Cooperative Eigenvalue Spectrum Sensing with a Realistic Receiver Model under Impulsive Noise," *Journal of Sensor and Actuator Networks*, vol. 2, pp. 46–69, 2013.

[9] X. Tan, W. Roberts, J. Li, and P. Stoica, "Sparse Learning via Iterative Minimization With Application to MIMO Radar Imaging," *IEEE Transactions on Signal Processing*, vol. 59, no. 3, pp. 1088–1101, 2011.

[10] A. Aubry, V. Carotenuto, A. De Maio, and M. A. Govoni, "Multi-Snapshot Spectrum Sensing for Cognitive Radar via Block-Sparsity Exploitation," *IEEE Transactions on Signal Processing*, vol. 67, no. 6, pp. 1396–1406, 2019.

[11] Z. Yang, J. Li, P. Stoica, and L. Xie, "Sparse Methods for Direction-Of-Arrival Estimation," in *Academic Press Library in Signal Processing, Volume 7*. Elsevier, 2018, pp. 509–581.

[12] J. A. Tropp and A. C. Gilbert, "Signal Recovery From Random Measurements Via Orthogonal Matching Pursuit," *IEEE Transactions on Information Theory*, vol. 53, no. 12, pp. 4655–4666, 2007.

[13] P. Babu and P. Stoica, "Multiple-Hypothesis Testing Rules for High-Dimensional Model Selection and Sparse-Parameter Estimation," *Signal Processing*, vol. 213, p. 109189, 2023.

[14] Z. Yang, C. Zhang, and L. Xie, "Robustly Stable Signal Recovery in Compressed Sensing With Structured Matrix Perturbation," *IEEE Transactions on Signal Processing*, vol. 60, no. 9, pp. 4658–4671, 2012.

[15] A. Aubry, A. De Maio, S. Marano, and M. Rosamilia, "Single-Pulse Simultaneous Target Detection and Angle Estimation in a Multichannel Phased Array Radar," *IEEE Transactions on Signal Processing*, vol. 68, pp. 6649–6664, 2020.

[16] M. Razaviyayn, M. Hong, and Z.-Q. Luo, "A Unified Convergence Analysis of Block Successive Minimization Methods for Nonsmooth Optimization," *SIAM Journal on Optimization*, vol. 23, no. 2, pp. 1126–1153, 2013.

[17] A. Aubry, A. De Maio, A. Zappone, M. Razaviyayn, and Z.-Q. Luo, "A New Sequential Optimization Procedure and Its Applications to Resource Allocation for Wireless Systems," *IEEE Transactions on Signal Processing*, vol. 66, no. 24, pp. 6518–6533, 2018.

[18] S. J. Wright, "Coordinate Descent Algorithms," *Mathematical programming*, vol. 151, no. 1, pp. 3–34, 2015.

[19] L. Han, X. Liu, N. Zhang, S. Wu, J. Zhu, and Z. Xu, "Two-Dimensional Multi-Snapshot Newtonized Orthogonal Matching Pursuit for DOA Estimation," *Digital Signal Processing*, vol. 121, p. 103313, 2022.